

# Evaluating the toughness of APS and HVOF-sprayed $\text{Al}_2\text{O}_3$ - $\text{ZrO}_2$ -coatings by in-situ- and macroscopic bending

J. Kiilakoski<sup>a,\*</sup>, R. Musalek<sup>b</sup>, F. Lukac<sup>b</sup>, H. Koivuluoto<sup>a</sup>, P. Vuoristo<sup>a</sup>

<sup>a</sup> Laboratory of Materials Science, Tampere University of Technology, Korkeakoulunkatu 6, 33720 Tampere, Finland

<sup>b</sup> Department of Materials Engineering, Institute of Plasma Physics CAS, v.v.i, Za Slovankou 3, 182 00 Praha 8, Czech Republic

\* Corresponding author. E-mail address: [jarkko.kiilakoski@tut.fi](mailto:jarkko.kiilakoski@tut.fi)

**Original article available at the Journal of the European Ceramic Society:**

<https://doi.org/10.1016/j.jeurceramsoc.2017.11.056>

## Abstract

Thermally-sprayed ceramic coatings are commonly used in applications where high wear and corrosion resistance are essential. However, their inherently low toughness and resistance to impacts often limit their use. In bulk ceramics, the toughening effect of  $\text{ZrO}_2$  has been successfully implemented in different compositions of  $\text{Al}_2\text{O}_3$ - $\text{ZrO}_2$ . Successful toughening leads to increased wear resistance and higher reliability. In this study, APS- and HVOF-sprayed  $\text{Al}_2\text{O}_3$ -40 $\text{ZrO}_2$  coatings were characterized with SEM and XRD techniques. The toughness of the coatings was evaluated by measuring their strain tolerance with in-situ (SEM) three-point-bending and macroscopic four-point bending with acoustic emission instrumentation. The APS-coatings had a higher strain-to-fracture but failed abruptly. In HVOF-coatings, the cracking commenced earlier but proceeded slower with more crack deflections. The observed behaviour is likely to derive from the coarser microstructure of the APS-coatings, which allows strain distribution in a larger area unlike the finer structure with a lesser melting degree of the HVOF-coatings.

Keywords: thermal spray;  $\text{Al}_2\text{O}_3$ - $\text{ZrO}_2$ ; toughening; fracture; mechanical testing

## 1. Introduction

Thermal spraying is widely used in creating thick protective or functional coatings on substrates of various materials. The coating is formed by melting the feedstock – typically powder or wire – and

propelling the droplets onto a surface where they impinge and solidify. Thermally sprayed ceramic coatings are often used in thermal barrier coatings (TBC), where stabilized  $\text{ZrO}_2$  is the most common material. Other oxides, such as  $\text{Al}_2\text{O}_3$ ,  $\text{Cr}_2\text{O}_3$ ,  $\text{TiO}_2$  are used in tribological applications requiring both wear and corrosion resistance. Examples of such applications are center press rolls of paper machines, process valves, mechanical seals etc. [1,2] Ceramic coatings have traditionally been sprayed with atmospheric plasma spray (APS) but recently, high-velocity oxy-fuel (HVOF) systems have been successfully used to produce dense, applicable and innovative coatings. [3] The main drawback of ceramic coatings has been their brittleness [4]. Therefore, increasing their fracture toughness without increasing the amount of defects in the structure is of great interest.

In the research of bulk ceramics,  $\text{ZrO}_2$  has been long known to exhibit high toughness [5], owing to both its ability to toughen due to the transformation from tetragonal to monoclinic phase as well as ferroelastic domain switching in the tetragonal phase. [6] A side effect of this phase change is a large volume increase which usually deteriorates the coating integrity. However, this can be countered by stabilizing the  $\text{ZrO}_2$  to either non-transformable tetragonal or cubic phases with additions of stabilizing oxides, such as  $\text{MgO}$  or  $\text{Y}_2\text{O}_3$  as is already widely utilized in top-coats of thermal barrier coatings, where the coatings resistance to catastrophic failure is critical due to immense cyclic thermo-mechanical loading. [1,7] Adjusting the amount of stabilizer allows for differing degrees of transformability, leading to the so-called partially stabilized zirconias (PSZ). [8]

Aluminium oxide is used in thermal spraying due to its low cost and ability to achieve sufficient mechanical and electric properties [9]. Efforts to incorporate the toughening effect of  $\text{ZrO}_2$  into the  $\text{Al}_2\text{O}_3$  coatings have been made recently [10–13]. Research on bulk ceramics has shown that already small additions of  $\text{ZrO}_2$  to  $\text{Al}_2\text{O}_3$  may result in improvements in fracture toughness compared to pure  $\text{Al}_2\text{O}_3$  [14–16]. For example, Chevalier et al. [14] have obtained a higher toughness for  $\text{Al}_2\text{O}_3$ -10 $\text{ZrO}_2$  (5.9  $\text{MPa}\sqrt{\text{m}}$ ) than either pure  $\text{Al}_2\text{O}_3$  (4.2  $\text{MPa}\sqrt{\text{m}}$ ) or pure  $\text{ZrO}_2$  (5.5  $\text{MPa}\sqrt{\text{m}}$ ).

It is known, that during the coating deposition the fast cooling of  $\text{Al}_2\text{O}_3$ - $\text{ZrO}_2$  readily leads to the formation of an amorphous phase [10,17], which Oberste Berghaus et al. [10] have found to reduce the mechanical strength and wear resistance of the coatings. On the other hand, in their study they also found that unlike in the case of APS spraying, the employment of HVOF-spraying lead to the retention of small  $\text{ZrO}_2$  particles in a matrix of  $\text{Al}_2\text{O}_3$ - $\text{ZrO}_2$ , which in turn improved the crack propagation resistance of the coating by over 30%. In various studies, Chen et al. utilized APS [11], suspension plasma spray (SPS) [11,12], and solution precursor high-velocity oxy-fuel spray (SPHVOF) [13] to deposit  $\text{Al}_2\text{O}_3$ - $\text{ZrO}_2$  -coatings. They were able to achieve an amorphous and nanocrystalline structure with high amounts of  $\alpha$ - $\text{Al}_2\text{O}_3$  and t- $\text{ZrO}_2$ .

It is a common practice to measure the toughness of thermally sprayed ceramic coatings by indentation measurements or four-point bend tests. [18] The drawback of using these tests is the required knowledge of elastic moduli and/or Poisson's ratio of the coating, which have their own difficulties of determining. Additionally, measuring values from only the coating in the four-point bending can prove difficult when testing a coated sample and not a free-standing coating. The addition of acoustic emission to the four-point bending experiment allows for further interpretation

of the cracking behaviour of a coating. This method has proven to be both repeatable [19] and informative [20–22]. Additional information has also been found from the traditional fracture toughness indentation test with the addition of acoustic emission instrumentation [23]. The understanding of these properties combined with wear testing of the coatings could lead to wholesome understanding of the damage tolerance of ceramic coatings, including resistance to macro- and micro-scale wear.

In the current study,  $\text{Al}_2\text{O}_3\text{-ZrO}_2$  coatings deposited with both APS and HVOF from two different feedstocks have been studied. The coatings were characterized by scanning electron microscopy (SEM) and X-ray diffraction, and their fracture characteristics were evaluated by four-point bending with acoustic emission (AE) monitoring and in-situ three-point bending in the SEM. The aim is to compare these novel toughness testing methods and to determine the applicability of the AE-instrumented four-point bending as a fast, robust way to determine coating toughness reliably. The effects of powder morphology and spray process on the coating properties are evaluated based on the results.

## 2. Experimental procedures

### 2.1 Materials and Coating Manufacturing

The coatings were prepared from two different feedstocks, a fused & crushed (F&C) powder (Ceram GmbH, Germany) and an agglomerated & sintered (A&S) powder (MilliDyne Oy, Finland). The latter was manufactured to the precise eutectic composition of the  $\text{Al}_2\text{O}_3\text{-ZrO}_2$  -system [24]. For the two spray methods, appropriate powder size distributions were used. The APS samples were sprayed using Oerlikon Metco F4MB atmospheric plasma spray system. The HVOF samples were sprayed with TopGun (GTV Verschleißschutz GmbH, Germany) with ethene as the fuel gas. The coatings were deposited on AISI 5120 low carbon steel plates which were grit-blasted with alumina (grit 36) before spraying. The samples for four-point bending were grit-blasted on both sides prior to spraying and their size was 180x25x5 mm. The deposition parameters are listed in Table 1.

Table 1 Spray parameters for the coating deposition

Sample name	APS F&C	APS A&S	HVOF F&C	HVOF A&S
Process	APS		HVOF	
Material Chemical Composition [wt.%]	$\text{Al}_2\text{O}_3\text{-40ZrO}_2$	$\text{Al}_2\text{O}_3\text{-42.5ZrO}_2$	$\text{Al}_2\text{O}_3\text{-40ZrO}_2$	$\text{Al}_2\text{O}_3\text{-42.5ZrO}_2$
Powder Manufacturer	Ceram	MilliDyne	Ceram	MilliDyne
Powder Size [Microns]	-51+20	-41+10	-30+10	-27+10
Current [A]	610		-	
Voltage [V]	70		-	
Power [kW]	42.7		-	
$\text{C}_2\text{H}_4$ [slpm]	-		90	
$\text{O}_2$ [slpm]	-		257	

Ar [slpm]	41		-	
H <sub>2</sub> [slpm]	13		-	
Standoff distance [mm]	140		150	
Relative surface speed [m/min]	87		179	
Offset [mm/pass]	7		2.9	
Passes [number]	36	48	36	30
Coating thickness [μm]	300	350	330	300

## 2.2 Microstructural and Mechanical Characterization

The powders and coatings were characterized by scanning electron microscopy and energy dispersive spectroscopy (SEM+EDS, Zeiss Evo 15, Zeiss GmbH, Germany and Philips XL30, FEI, Eindhoven, The Netherlands). X-ray diffraction with quantitative Rietveld refinement phase analysis [25] of the feedstock powders and coatings was performed by TOPAS v5 software on data acquired by D8 Discover XRD [26] (Bruker, Karlsruhe, Cu-K $\alpha$  radiation of wavelength 1.5406 Å, Germany). The microhardness of the coatings was measured from ten indentations using a Vickers hardness tester (MMT-X7, Matsuzawa, Japan) and a load of 300 gf (HV<sub>0.3</sub>). The coating porosities were estimated from six cross-sectional SEM micrographs using back-scattered electron (BSE) imaging mode and three different magnifications (1000x, 3000x and 5000x), two images per each magnification.

## 2.3 Four-point bending with acoustic emission instrumentation

A universal testing machine (Instron 8800, Norwood, MA, USA) was utilized with a 100 kN load cell and a four-point bending jig. In the jig, the inner span of the support pins was 45 mm and for the outer pins 110 mm. The samples were tested with the coating in tension facing downwards and a piezoelectric sensor (8313, Bruel & Kjaer, Denmark) with a resonance frequency of 200 kHz was attached to the substrate side of the sample to detect the elastic waves initiated by coating failure. A schematic presentation of the experimental setup is presented in Fig.1. Four samples of each coating were tested. The AE-sensor was attached via a preamplifier (2637, Bruel & Kjaer, Denmark) to a data acquisition unit (NI cDAQ9174 and NI9223, National Instruments, USA) that was connected to a computer. The sampling frequency was 1 MHz. The acquired data was analysed with the DIAdem-software (National Instruments, USA).

The samples were bent with a speed of 10 mm/min, until the central support displacement of 10 mm was reached. This led to a displacement of 14.0±0.5 mm at mid-span of the samples. The acoustic energy E<sub>AE</sub> emitted during bending was calculated according to Equation 1 [27]

$$E_{AE} = \frac{1}{R} \int_{t_1}^{t_2} V(t)^2 dt \quad (\text{Eq. 1})$$

where  $R$  is the electrical resistance of the preamplifier (10 kΩ is chosen per convention) and  $V$  is the amplitude of the signal. Two uncoated samples were also bent and the total energy averaged. This value was kept as a reference threshold value for the bend tests; when the total acoustic energy of a coated sample surpasses this threshold value, the strain is marked as “strain-to-fracture”. The

surface strain value is calculated from the displacement using beam theory according to Equation 2 [28]

$$\varepsilon[\%] = \frac{436Dh}{L^2}, \quad (\text{Eq. 2})$$

where  $D$  is displacement at mid-span in mm,  $h$  is the thickness of the sample and  $L$  is the distance of the outer pins. Graphs of a raw AE-signal vs. time for an uncoated and coated sample are illustrated in Fig. 2.

## 2.4 In-situ three-point bending

In-situ three-point bending was carried out in low vacuum mode in SEM microscope EVO MA 15 (Carl Zeiss SMT, Germany) equipped with Microtest 200 N tensile tester (Deben, UK). BSE imaging was used in order to obtain desired phase contrast. Three-point bending setup with outer support span of 23 mm was used. Samples for testing were cut from the as-sprayed samples with a metallographic precision saw and ground in order to remove any material possibly damaged during cutting and assure proper geometry of the samples and planarity of the cuts. Substrate was thinned by grinding in order to decrease stiffness of the samples. Cross-section to be observed was polished using a standard materialographic procedure up to an oxide polishing stage using colloidal silica (OP-S). Dimensions of the final beams were approximately 1.5 x 1.5 x 30 mm (width x thickness x length), with the thickness of the coating remaining as sprayed, i.e. 0.3-0.35 mm and the thickness of the substrate being 1.15-1.2 mm. Samples were loaded with the coating in tension, displacement rate of central support of 0.1 mm/min and interrupted “stepwise” loading mode [29], i.e., at predefined displacements, loading was stopped and the ongoing materials failure was documented with acquisition of high-resolution image. From the time-lapse sequence of such micrographs, failure propagation may be studied. For each coating, three samples were tested with repeatable results. More details on the testing method are presented in [29–31]. The distances between cracks were measured by selecting the two adjacent cracks next to the magistrate crack that was created in the middle of the sample where the support pin was. These two distances were measured for all samples and presented as an average of six measurements.

## 3. Results & Discussion

### 3.1 The powder morphology

The powder morphologies are presented in Fig. 3. Two phases can be clearly distinguished from differing shades of grey in the images;  $\text{ZrO}_2$  is brighter due to the greater atomic number of Zr in  $\text{ZrO}_2$  than Al in  $\text{Al}_2\text{O}_3$ . The fused & crushed powders are of irregular shape with sharp facets and fully dense while the agglomerated & sintered powders are spherical and somewhat porous. The morphology of the particles resulting from spray drying is very variable with artefacts such as blowholes that, when large enough, can resemble a donut. [32] The blowholes can be formed during spray drying for example due to the evaporation rate of the solvent exceeding the rate of liquid/vapour diffusion through the particle, thus rupturing the particle wall. [33] Generally, in the



F&C powder, most particles are a mixture of  $\text{Al}_2\text{O}_3$  and  $\text{ZrO}_2$  but particles consisting of only one material can be seen as well in Fig. 3a) and c). On the contrary, the nature of agglomeration and much finer size of the  $\text{Al}_2\text{O}_3$  and  $\text{ZrO}_2$  regions in the A&S powders enables the more homogeneous mixing of both constituents in the particles – see Fig. 3b) and d).

### 3.2 The coating microstructure

The cross-sectional structures of the APS-coatings, APS F&C and APS A&S, are presented in Fig. 4. Both coatings are relatively dense with  $2.18 \pm 0.38$  % and  $2.03 \pm 0.45$  % total porosity, respectively, while presenting some minor vertical quenching cracks. Presence of such intrasplat cracks is a typical result of residual stress relaxation in the ceramic coatings [34]. The gradient shades of grey coming from the different Al:Zr ratio in the individual splats indicate effective intermixing and merging of the original  $\text{Al}_2\text{O}_3$  and  $\text{ZrO}_2$  phases present in the feedstock powders in various contents possibly forming nanocrystalline or even amorphous splats which is common in thermal spraying of  $\text{Al}_2\text{O}_3$ - $\text{ZrO}_2$  coatings [17]. The elemental map of Fig. 4b) obtained by EDS is presented in Fig. 5, where the Zr- and Al-rich areas can easily be distinguished. The APS-coating sprayed with the agglomerated & sintered powder has more unmelted particles, Fig. 4d. Generally, the distinct separation of large areas of different phases in the fused & crushed powder has led to a more pronounced heterogeneous structure in the coating with  $\text{Al}_2\text{O}_3$ -rich,  $\text{ZrO}_2$ -rich and mixed regions.

Presented in Fig. 6 are the cross-section images of the F&C and A&S HVOF –coatings. Similar to their APS counterparts, also here the coating sprayed from the agglomerated & sintered powder the coating has a more homogeneous phase distribution. The coating HVOF A&S has a high density of vertical cracks – similar to both APS coatings – while the fused & crushed powder leads to a seemingly more dense structure in the coating HVOF F&C. However, the total porosities of the F&C and A&S coatings were  $1.16 \pm 0.35$  % and  $0.88 \pm 0.31$  %, respectively. In addition, due to the finer feedstock powder, both coatings exhibit a finer microstructure in comparison with the plasma-sprayed coatings.

The difference in splat sizes can also be verified from the surface images presented in Fig. 7., where the finer size of the splats can be seen in the HVOF coatings. Additionally, the amount of cracking in the F&C HVOF coating is also on the free surfaces lower than in all other coatings.

Vickers hardnesses of the coating cross-sections are plotted along with the coating porosities in the graph in Fig. 8. The hardness values reflect well the above mentioned differences in the coating microstructure. The agglomerated & sintered powders resulted in slightly more vertical cracking in the coatings and therefore a weaker structure. Low porosity and a defect-free structure can lead to higher hardnesses [2], which is also presented by the high hardness value of  $917 \pm 48$   $\text{HV}_{0.3}$  of the seemingly dense HVOF-sprayed F&C-coating. The porosities of the coatings are on the lower end of typical porosity values of these thermal spray methods [1] and are largely a result of the spherical pores and microcracks as seen in Fig. 4 and Fig. 6. Noteworthy is the distinction between the porosities of F&C and A&S –coatings; with both spray methods the F&C coatings exhibited higher porosities, but this small difference is likely due to the darker regions in the coating cross-sections causing error in the measurement due to its visual nature.

Quantitative Rietveld refinement analysis was performed on the XRD profiles of the samples in order to determine the phase compositions of the feedstock powders and resulting coatings. The compositions extracted from the analyses are presented in Table 2. All feedstock powders were fully crystalline and exhibited similar phase compositions close to the eutectic composition 61.8 mol-%  $\alpha$ - $\text{Al}_2\text{O}_3$  with the balance being mainly monoclinic  $\text{ZrO}_2$ . A graph of the XRD scans of the powders is presented in Fig. 9.

Table 2 Phase compositions of the feedstock and the coatings as calculated from the Rietveld analysis.

		APS F&C		APS A&S		HVOF F&C		HVOF A&S	
		Feedstock	Coating	Feedstock	Coating	Feedstock	Coating	Feedstock	Coating
Crystallinity [%]		100	45	100	15	100	46	100	18
Phase content [mol-%]	$\alpha$ - $\text{Al}_2\text{O}_3$	64,3 $\pm 0,5$	17,3 $\pm 0,5$	62,0 $\pm 0,2$	61,1 $\pm 0,5$	63 $\pm 1$	27,5 $\pm 0,5$	62,0 $\pm 0,7$	43,8 $\pm 0,5$
	$\gamma$ - $\text{Al}_2\text{O}_3$	-	24 $\pm 1$	-	-	-	11 $\pm 1$	-	-
	t- $\text{ZrO}_2$	1,3 $\pm 0,1$	18 $\pm 1$	1,13 $\pm 0,05$	8 $\pm 1$	1,4 $\pm 0,1$	25 $\pm 1$	1,11 $\pm 0,06$	4 $\pm 1$
	m- $\text{ZrO}_2$	34,4 $\pm 0,5$	40 $\pm 1$	36,9 $\pm 0,2$	30 $\pm 1$	36 $\pm 1$	36 $\pm 1$	36,9 $\pm 0,7$	52 $\pm 1$

The phase composition of the coatings was more variable, their diffraction pattern fits are presented in Fig. 10. Both F&C coatings consisted of  $\alpha$ - and  $\gamma$ - $\text{Al}_2\text{O}_3$  and monoclinic and tetragonal  $\text{ZrO}_2$ . The amounts of both  $\alpha$ - $\text{Al}_2\text{O}_3$  and t- $\text{ZrO}_2$  were higher in the HVOF coating. The composition difference is likely due to the lower temperature of the HVOF-process leading to the temperature of the coating dropping under the transition temperature faster, which enables higher retention of the tetragonal  $\text{ZrO}_2$ . The t- $\text{ZrO}_2$  was found to be transformable, as investigated by calculating the  $c/a\sqrt{2}$  -ratio of the unit cell. The ratio was 1.02 for APS F&C and 1.019 for HVOF F&C, which are far from the ratio of non-transformable t'- $\text{ZrO}_2$  found to be between 1.005 [35] and 1.01 [36]. Additionally, the coatings had a crystallinity of 45-46 % indicating large amounts nanocrystalline or amorphous phases.

The A&S coatings consisted of  $\alpha$ - $\text{Al}_2\text{O}_3$ , m- $\text{ZrO}_2$  and t- $\text{ZrO}_2$  with a crystallinity of only 15 and 18 % for the APS and HVOF coatings, respectively. Hence, the coating is mainly amorphous and determination of the phase content is difficult. Moreover, due to the low amount of t- $\text{ZrO}_2$  we were not able to calculate the amount of t'- $\text{ZrO}_2$  for the A&S samples. The low amount of t- $\text{ZrO}_2$  in the A&S coatings can be credited to the feedstock being unstabilized. Interestingly, the lower amount of  $\alpha$ - $\text{Al}_2\text{O}_3$  in the HVOF A&S coating as compared to APS A&S coating indicates that a higher amount of  $\text{Al}_2\text{O}_3$  was in nanocrystalline or amorphous form, possibly stemming from a combined effect of smaller particle-size and lower process temperature. The low crystallinity in the A&S coatings is likely due to the well mixed finer primary particles of  $\text{Al}_2\text{O}_3$  and  $\text{ZrO}_2$ , where the  $\text{Al}_2\text{O}_3$  particles can slow the crystallization of  $\text{ZrO}_2$  nanoparticles from amorphous  $\text{ZrO}_2$  [37].

### 3.3 In-situ SEM three-point bending

During the *in-situ* bending experiment, evolution of the coating failure was observed [dataset] [38]. The macroscopic fracture behaviour of all the tested coatings was similar. First, several short cracks initiated above the central loading pin at the free surface of the coating, where the maximum strain was imposed. From the deflection of the sample, critical flexural strain at the coating surface was evaluated (see Fig. 11). In general, critical flexural strain of both APS samples was about 20 % higher than for HVOF coatings. As the straining increased, cracks propagated in the through-thickness direction but shortly, only one crack became dominant causing localized strain relief in the surrounding material and thus retarding and then even closing the other nearby cracks. Hence, only one main through-thickness crack usually emerged above the central loading pin.

This main crack propagated almost perpendicularly to the free surface. After reaching the substrate, it diverted and propagated along the coating-substrate interface causing large-scale delamination of the coating. Straining of the partially delaminated coating could in the areas of improved mechanical anchoring lead to localized formation of short cracks originating at the coating-substrate interface and propagating towards the sample surface. This was observable especially for the HVOF A&S -coating (see Fig. 12). With further bending, secondary through-thickness cracks were also developed from the free surface (see HVOF A&S in Fig. 12d). Note that for the other samples in Fig. 12, the secondary cracking was out of observable area. Spacing between the through-thickness cracks was found to be strongly dependent on the thermal spray process, being about two-times higher for plasma spraying than for HVOF (Fig. 11) Together with higher critical flexural strain, it indicates that the coarser and looser microstructure of APS samples was more effectively accommodating the imposed straining, which thus resulted in the improved macroscopic strain-tolerance. This behaviour corresponds to earlier observations by Musalek et al. in the earlier works [39,40].

During the *in-situ* bending, all four tested coatings also showed excellent internal cohesion. In general, regardless of the local phase composition, cracks did not follow the splat-splat interfaces but cracking of the splats and interlinking of the original short vertical quenching cracks (see Fig. 13) were dominant micromechanisms of the crack propagation. As denoted by numbers in Fig. 12, in all cases the crack initiated at the free surface of the coating making its way towards the substrate-coating interface instantaneously (1). In both APS coatings and the HVOF F&C coating this was followed by interface opening and onset of the coating delamination (2). When suitable conditions arose (usually at a weak link in the coating and/or a peak in the substrate topography) the newly formed cracks propagated back into the coating toward the free surface (3). In the case of HVOF A&S coating the bond strength was sufficient to withstand crack propagation and the second type of cracking was suppressed. It should be noted that the coating damage was most prominent in the crack initiation area, distinguishable within about 20 microns distance from the major cracks (Fig. 13) leaving most of the surrounding coating intact.

### 3.4 Four-point bending

The results of the four-point bending test with acoustic emission instrumentation are presented in Fig. 14. In general, the APS-coatings showed again a higher strain tolerance when compared to the



HVOF-coatings, which can be attributed to the coarser microstructure of the APS coatings and their higher internal cohesion that is able to more efficiently accommodate the imposed tensile straining. In other words, the smaller splat size of the HVOF-coatings and their denser yet partially less melted structure leads to the cracking accommodating stresses only in the near region of the crack. This is confirmed by the similar trend observed from the in-situ three-point bending, where APS coatings had a higher strain at the appearance of the first visible crack. The measured strain is higher in four-point bending than in three-point bending, since in the latter, the very first visible crack is recorded while in the four-point bending test, crossing of cumulative noise threshold is recorded as cracking. When comparing the coatings deposited with the same spray-method, the F&C-coatings has a higher strain tolerance and lower variation than the A&S coatings. This is likely a result of the more crystalline structure and hence more available slip planes of the F&C coatings. Furthermore, the variation in the results of the test correlates with coating homogeneity and the amount of glassy phase. The scatter is higher for APS- than HVOF-coatings, and for the A&S- than F&C-powders. Comparison with the scatter in the in-situ bending results reveals again similarity in the HVOF F&C coating having clearly the lowest scatter and in general, the A&S coating had vastly larger variation in test results.

Analyses of the power spectrum densities were performed for the FFT-transformed signals. This allows us to evaluate the amplitude of the signal at different frequencies, rather than just against a time-scale [41]. Comparison between the coatings is presented in a normalized histogram with a bin size of 50 kHz and 25 kHz near the resonant frequency of the sensor at 200 kHz in Fig. 15 highlighting the characteristic frequencies recorded during bending. This enables us to compare the dynamics of the cracking in the coatings, since a more rapid crack propagation should lead to a higher frequency elastic wave in the substrate while more crack deflections and a longer crack path should lead to a lower detected frequency.

An interesting finding is that the HVOF-coatings tend to show more intensive cracking in the lower frequency range of 100-150 kHz than the APS-coatings while there is more cracking in the range 200-250 kHz in the latter. A possible explanation is that the higher melting degree and coarser microstructure of the APS coatings lead to stronger but fewer inter-splat connections and that the cracking occurs more abruptly and violently, causing a higher frequency elastic wave in the sample. On the other hand, the smaller scale microstructure and unmelted areas in the HVOF-coatings lead to a more gradual crack opening, which causes waves of lower frequencies. Similar observations were made by Driver et al. [42], who attributed lower energy acoustic emission during bending of HVOF-sprayed WC-17Co -coatings to the pre-existing cracks and their subsequent opening as opposed to well-molten structures where cracks are forced to propagate through the splats. An analysis of the acoustic wave geometry from bending YSZ thermal barrier coatings was performed by Ma et al. [20], where shorter rise time (higher frequency) was attributed to local fracture of a weak area in the coating and a longer rise time (lower frequency) was due to a slip in the coating or at the coating/substrate interface. This is analogous to the difference between ductile tearing and brittle fracture, as was also noticed earlier by Akita et al. [43] in their study of APS-sprayed Mo-coatings. They claimed that greater energy released stems from a more ductile coating, but the apparent

contradiction to our findings is due to a different definition of ductility for a ceramic coating. Akita et al. defined ductility as the ability to resist microcracking, while in the current work, “tougher” behaviour means resisting catastrophic failure to greater strains since microcracks are generated already during deposition. Additionally, Tronskar et al. [44] found in impact testing of normalized ship grade steels that ductile tearing causes acoustic noise in a broader spectrum of frequencies, with the maximum peak significantly lower than in brittle fracture. This also gives assurance to our presumption that the APS coatings are more brittle due to their higher melting degree, while HVOF coatings are toughened by the pre-existing microcracks and unmelted areas. This idea is supported by the crack distances measured in the in-situ bending test (Fig. 11), where the pre-existing cracks of the HVOF-coatings led generally to smaller distances between newly formed through-thickness cracks than in the APS-coatings.

Another observation can be made of the difference between F&C and A&S coatings: there are fewer impulses in the 175-200 kHz frequency range in the A&S coatings than the F&C counterparts, while there are more impulses for the A&S coatings in the 200-225 kHz range. The difference is greater in the case of HVOF than APS, possibly due to the lower melting power of the HVOF-process emphasizing the effect of the difference in powder type. In practice, this difference is quite negligible considering the physical phenomenon and that the resonant frequency of the sensor is at 200 kHz.

#### 4. Conclusion

In this study, APS and HVOF-sprayed  $\text{Al}_2\text{O}_3\text{-}40\text{ZrO}_2$  coatings from eutectic F&C and A&S feedstocks were deposited and examined in regards to their behaviour in tensile loading in bending with two methods: in-situ three-point bending and macroscopic AE-instrumented four-point bending.

During *in-situ* bending, the cracking mechanism between different coatings did not show significant differences, except for HVOF-sprayed A&S coating that had numerous pre-existing cracks. The newly formed through thickness cracks were significantly further apart in the APS-coatings than the HVOF-coatings, indicating a greater capability of the coarser microstructure of the APS-coatings to accommodate stresses. This is also evidenced in their lower hardness values. The flexural strain from the in-situ experiment was significantly smaller than from AE, but both tests gave similar trends. The difference in detected strain is due to the difference in the method of failure detection. During the *in-situ* experiment, the onset of the individual cracks could be detected whereas the AE-method is sensitive to extensive coating failure, which produces acoustic energy strong enough to reach the predefined threshold energy value.

Using the F&C feedstock generally led to a higher strain tolerance, although the scatter in the case of A&S-coatings was quite high. The amorphous nature of the A&S coatings likely leads to the low strain-tolerance due to the absence of available slip planes. The variation in both tests was quite high, which was observed to be higher for coatings with a larger number of pre-existing faults. Thus, variation in these tests seems to be also a good indicator of coating quality.

The spectra of the AE-signals showed a difference in the characteristic frequency of cracking between APS and HVOF-coatings. The APS-coatings cracked more abruptly causing a higher

frequency impulse, while the HVOF-coatings had more low frequency cracks probably stemming from the higher density of pre-existing cracks and unmelted particles as well as a smaller microstructural scale leading to more crack deflections. Therefore, the crack propagation in the HVOF-coatings happened more gradually.

With the help of in-situ three-point bending observations, the AE-instrumented four-point bending was validated to be a good measure of coating quality and able to detect even slight differences in toughness stemming from the coating structure. It can therefore be considered as one more method alongside the existing ones in evaluating the toughness of thermally sprayed ceramic coatings.

Further work on the topic should focus on expanding the amount and types of materials tested with four-point-bending to obtain a broader view of the toughness values in different compositions of thermally sprayed coatings.

## Acknowledgements

The work was supported by DIMECC Ltd, its HYBRIDS programme and Tekes (Finnish Funding Agency for Technology and Innovation). In-situ testing was supported through grant GB14-36566G “Multidisciplinary research centre for advanced materials” (Czech Science Foundation). The authors would like to thank Mr. Mikko Kylmälahti of Tampere University of Technology for spraying the coatings.

## References

- [1] P. Vuoristo, Thermal Spray Coating Processes, in: S. Hashmi (Ed.), Comprehensive Materials Processing Vol. 4, Elsevier, 2014, pp. 229–276. doi:10.1016/B978-0-08-096532-1.00407-6.
- [2] L. Pawlowski, The Science and Engineering of Thermal Spray Coatings, second ed., John Wiley & Sons, West Sussex, England, 2008. doi:10.1002/9780470754085.
- [3] P.L. Fauchais, J.V.R. Heberlein, M.I. Boulos, Thermal Spray Fundamentals, Springer US, Boston, MA, 2014. doi:10.1007/978-0-387-68991-3.
- [4] G. Bolelli, V. Cannillo, L. Lusvarghi, T. Manfredini, Wear behaviour of thermally sprayed ceramic oxide coatings, Wear. 261 (2006) 1298–1315. doi:10.1016/j.wear.2006.03.023.
- [5] A. Evans, Perspective on the Development of High-Toughness Ceramics, J. Am. Ceram. Soc. 73 (1990) 187–206. doi:10.1111/j.1151-2916.1990.tb06493.x.
- [6] G. V. Srinivasan, J.F. Jue, S.Y. Kuo, A. V. Virkar, Ferroelastic domain switching in polydomain tetragonal zirconia single crystals, J. Am. Ceram. Soc. 72 (1989) 2098–2103. doi:10.1111/j.1151-2916.1989.tb06038.x.

- [7] R.A. Miller, Thermal barrier coatings for aircraft engines: History and directions, *J. Therm. Spray Technol.* 6 (1997) 35–42. doi:10.1007/BF02646310.
- [8] J.R. Kelly, I. Denry, Stabilized zirconia as a structural ceramic: An overview, *Dent. Mater.* 24 (2008) 289–298. doi:10.1016/j.dental.2007.05.005.
- [9] J. Ilavsky, C. Berndt, H. Herman, Alumina-base plasma-sprayed materials—Part II: Phase transformations in aluminas, *J. Therm. Spray Technol.* 6 (1997) 439–444. doi:10.1007/s11666-997-0028-2.
- [10] J. Oberste Berghaus, J.-G. Legoux, C. Moreau, F. Tarasi, T. Chráska, Mechanical and Thermal Transport Properties of Suspension Thermal-Sprayed Alumina-Zirconia Composite Coatings, *J. Therm. Spray Technol.* 17 (2007) 91–104. doi:10.1007/s11666-007-9146-0.
- [11] D. Chen, E.H. Jordan, M. Gell, Microstructure of Suspension Plasma Spray and Air Plasma Spray Al<sub>2</sub>O<sub>3</sub>-ZrO<sub>2</sub> Composite Coatings, *J. Therm. Spray Technol.* 18 (2009) 421–426. doi:10.1007/s11666-009-9306-5.
- [12] D. Chen, E.H. Jordan, M. Gell, Suspension plasma sprayed composite coating using amorphous powder feedstock, *Appl. Surf. Sci.* 255 (2009) 5935–5938. doi:10.1016/j.apsusc.2009.01.038.
- [13] D. Chen, E.H. Jordan, M. Gell, Solution precursor high-velocity oxy-fuel spray ceramic coatings, *J. Eur. Ceram. Soc.* 29 (2009) 3349–3353. doi:10.1016/j.jeurceramsoc.2009.07.010.
- [14] J. Chevalier, A.H. De Aza, G. Fantozzi, M. Schehl, R. Torrecillas, Extending the lifetime of ceramic orthopaedic implants, *Adv. Mater.* 12 (2000) 1619–1621. doi:10.1002/1521-4095(200011)12:21<1619::AID-ADMA1619>3.0.CO;2-O.
- [15] J. Chevalier, S. Deville, G. Fantozzi, J.F. Bartolomé, C. Pecharroman, J.S. Moya, et al., Nanostructured ceramic oxides with a slow crack growth resistance close to covalent materials, *Nano Lett.* 5 (2005) 1297–1301. doi:10.1021/nl050492j.
- [16] E. Kannisto, M.E. Cura, E. Levänen, S.P. Hannula, Mechanical Properties of Alumina Based Nanocomposites, *Key Eng. Mater.* 527 (2012) 101–106. doi:10.4028/www.scientific.net/KEM.527.101.
- [17] H.-J. Kim, Y.J. Kim, Amorphous phase formation of the pseudo-binary Al<sub>2</sub>O<sub>3</sub>-ZrO<sub>2</sub> alloy during plasma spray processing, *J. Mater. Sci.* 34 (1999) 29–33. doi:10.1023/A:1004492919174.
- [18] A.S.M. Ang, C.C. Berndt, A review of testing methods for thermal spray coatings, *Int. Mater. Rev.* 59 (2014) 179–223. doi:10.1179/1743280414Y.0000000029.
- [19] L.C. Cox, The four-point bend test as a tool for coating characterization, *Surf. Coatings Technol.* 36 (1988) 807–815. doi:10.1016/0257-8972(88)90021-7.

- [20] X.Q. Ma, S. Cho, M. Takemoto, Acoustic emission source analysis of plasma sprayed thermal barrier coatings during four-point bend tests, *Surf. Coat. Technol.* 139 (2001) 55–62. doi:10.1016/S0257-8972(01)00995-1.
- [21] L. Yang, Z.C. Zhong, J. You, Q.M. Zhang, Y.C. Zhou, W.Z. Tang, Acoustic emission evaluation of fracture characteristics in thermal barrier coatings under bending, *Surf. Coat. Technol.* 232 (2013) 710–718. doi:10.1016/j.surfcoat.2013.06.085.
- [22] E. Mayrhofer, L. Janka, W.P. Mayr, J. Norpoth, M.R. Ripoll, M. Gröschl, Cracking resistance of Cr<sub>3</sub>C<sub>2</sub>–NiCr and WC–Cr<sub>3</sub>C<sub>2</sub>–Ni thermally sprayed coatings under tensile bending stress, *Surf. Coat. Technol.* 281 (2015) 169–175. doi:10.1016/j.surfcoat.2015.09.002.
- [23] E. Smazalová, Š. Houdková, The Potential of AE Sensing in the Indentation Fracture Toughness Measurement, in: P. Louda, (Ed.), *Defect and Diffusion Forum Vol. 368*, Trans Tech Publications, Zürich, Switzerland, 2016, pp. 203–206. doi:10.4028/www.scientific.net/DDF.368.203.
- [24] G.R. Fischer, L.J. Manfredo, R.N. McNally, R.C. Doman, The eutectic and liquidus in the Al<sub>2</sub>O<sub>3</sub> - ZrO<sub>2</sub> system, *J. Mater. Sci.* 16 (1981) 3447–3451.
- [25] H.M. Rietveld, Line profiles of neutron powder-diffraction peaks for structure refinement, *Acta Crystallogr.* 22 (1967) 151–152. doi:10.1107/S0365110X67000234.
- [26] A.A. Coelho, TOPAS version 5 (Computer Software), (2016).
- [27] M. Löhr, D. Spaltmann, S. Binkowski, E. Santner, M. Woydt, In situ Acoustic Emission for wear life detection of DLC coatings during slip-rolling friction, *Wear.* 260 (2006) 469–478. doi:10.1016/j.wear.2005.03.009.
- [28] J. Voyer, H. Kreye, Determination of cracking resistance of thermal spray coatings during four-point bend testing using an acoustic emission technique, *J. Therm. Spray Technol.* 12 (2003) 416–426. doi:10.1361/105996303770348285.
- [29] R. Musalek, C. Taltavull, A.J. Lopez Galisteo, N. Curry, Evaluation of failure micromechanisms of advanced thermal spray coatings by in-situ experiment, *Key Eng. Mater.* 606 (2014) 187–190. doi:10.4028/www.scientific.net/KEM.606.187.
- [30] R. Musalek, M. Vilemova, J. Matejcek, U. Rey, J. Carlos, In-situ Observation of Ongoing Microstructural Changes in Functionally Graded Thermal Spray Coating during Mechanical Loading, in: T.S. Sudarshan, P. Vuoristo, H. Koivuluoto (Eds.), *Surf. Modif. Technol. XXVIII*, Valardocs, Tampere, Finland, 2014, pp. 571–579.
- [31] R. Mušálek, O. Kovářík, J. Matějčík, In-situ observation of crack propagation in thermally sprayed coatings, *Surf. Coat. Technol.* 205 (2010) 1807–1811. doi:10.1016/j.surfcoat.2010.03.064.
- [32] P. Fauchais, G. Montavon, G. Bertrand, From powders to thermally sprayed coatings, *J. Therm. Spray Technol.* 19 (2010) 56–80. doi:10.1007/s11666-009-9435-x.



- [33] D.E. Walton, C.J. Mumford, Spray Dried Products - Characterization Of Particle Morphology, Trans. Inst. Chem. Eng. 77 (1999) 21–38.
- [34] S. Kuroda, T.W. Clyne, The quenching stress in thermally sprayed coatings, Thin Solid Films. 200 (1991) 49–66. doi:10.1016/0040-6090(91)90029-W.
- [35] M. Leoni, R. Jones, P. Scardi, Phase stability of scandia–yttria-stabilized zirconia TBCs, Surf. Coat. Technol. 108 (1998) 107–113. doi:10.1016/S0257-8972(98)00617-3.
- [36] C. Viazzi, J.-P. Bonino, F. Ansart, A. Barnabé, Structural study of metastable tetragonal YSZ powders produced via a sol–gel route, J. Alloys Compd. 452 (2008) 377–383. doi:10.1016/j.jallcom.2006.10.155.
- [37] B.L. Kirsch, A.E. Riley, A.F. Gross, S.H. Tolbert, Probing the Effects of Interfacial Chemistry on the Kinetics of Phase Transitions in Amorphous and Tetragonal Zirconia Nanocrystals, Langmuir. 20 (2004) 11247–11254. doi:10.1021/la048343o.
- [dataset] [38] R. Musalek, In-situ SEM observation of crack propagation in Al<sub>2</sub>O<sub>3</sub>-ZrO<sub>2</sub> APS and HVOF coatings, Mendeley Data, v1, 2017. doi:10.17632/szs2dm95vn.1.
- [39] R. Musalek, J. Matejcek, M. Vilemova, O. Kovarik, Non-Linear Mechanical Behavior of Plasma Sprayed Alumina Under Mechanical and Thermal Loading, J. Therm. Spray Technol. 19 (2009) 422–428. doi:10.1007/s11666-009-9362-x.
- [40] R. Mušálek, J. Matějček, V. Pejchal, E. Mari, a Valarezo, S. Sampath, Influence of Pores and Cracks Morphology on Mechanical Behavior of Thermally Sprayed Ceramics, in: B.R. Marple, A. Agarwal, M.M. Hyland, Y.-C. Lau, C.-J. Li, R.S. Lima, G. Montavon (Eds.), Proceedings of the International Thermal Spray Conference, DVS Media GmbH, Singapore, 2010, 723–728.
- [41] A. Brandt, Noise and Vibration Analysis: Signal Analysis and Experimental Procedures, 1st ed., John Wiley & Sons, Inc., New Jersey, United States, 2010.
- [42] L.C. Driver, P.H. Shipway, D.G. McCartney, Acoustic Emission as a Tool for Characterising HVOF-Sprayed WC-Co Coatings, in: B.R. Marple, C. Moreau (Eds.), Thermal Spray 2003: Advancing the Science And Applying the Technology, ASM International, Orlando, USA, 2003, pp. 801–807.
- [43] K. Akita, G. Gang, S. Takahashi, H. Misawa, S. Tobe, In-situ observation and AE analysis of microscopic fracture process of thermal spray coatings.pdf, in: C. Coddet (Ed.), Proc. 15th Int. Therm. Spray Conf., ASM International, Nice, France, 1998, pp. 837–842.
- [44] J.P. Tronskar, M.A. Mannan, M.O. Lai, Application of Acoustic Emission for Measuring Crack Initiation Toughness in Instrumented Charpy Impact Testing, J. Test. Eval. 31 (2003) 222–233. doi:10.1520/JTE12420J.

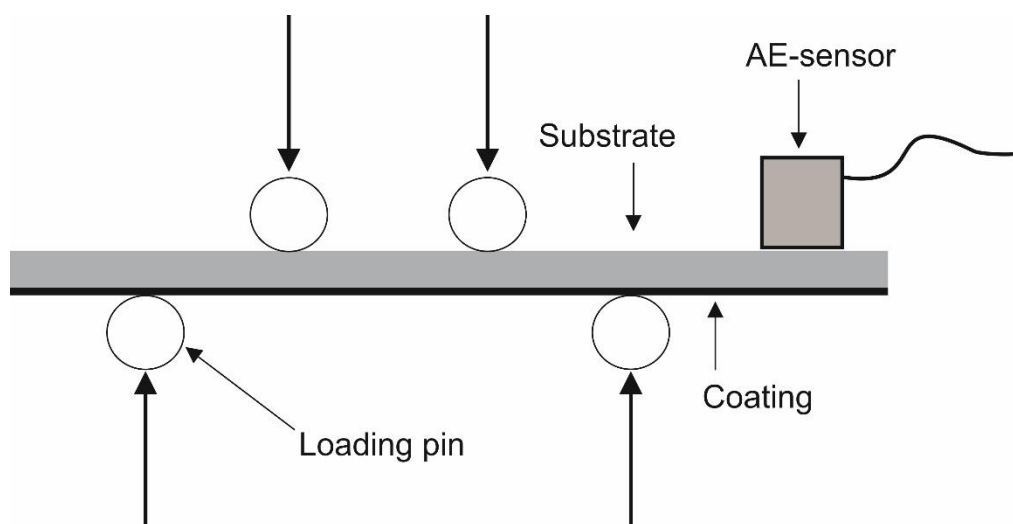


Fig.1 A schematic of the experimental setup of the four-point bending.

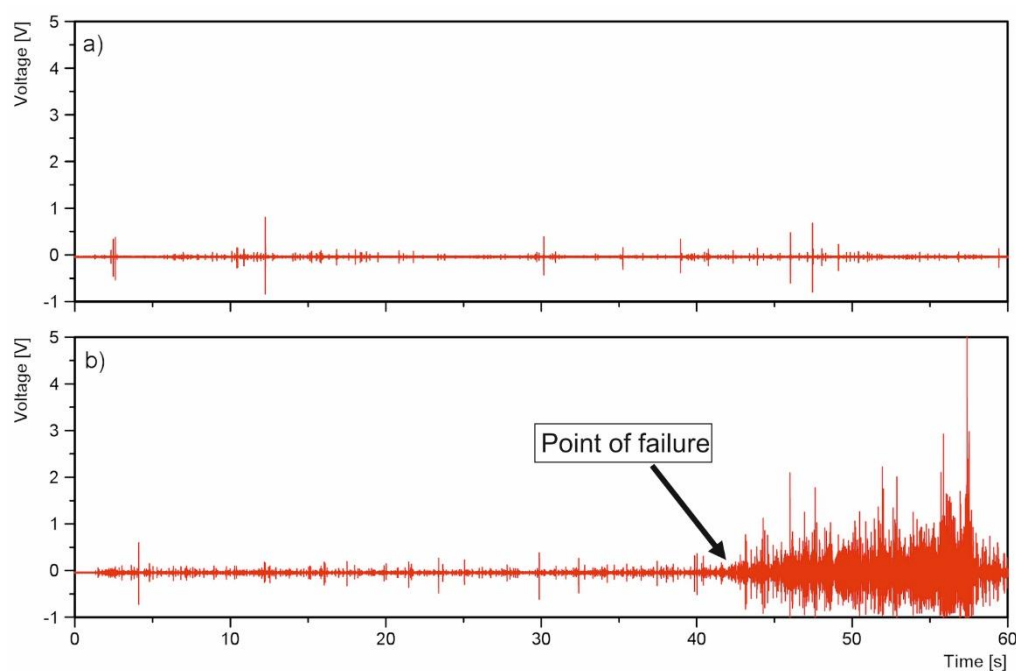


Fig. 2. Graphs of the AE-signal vs. time of a) uncoated and b) coated sample during four-point-bending.

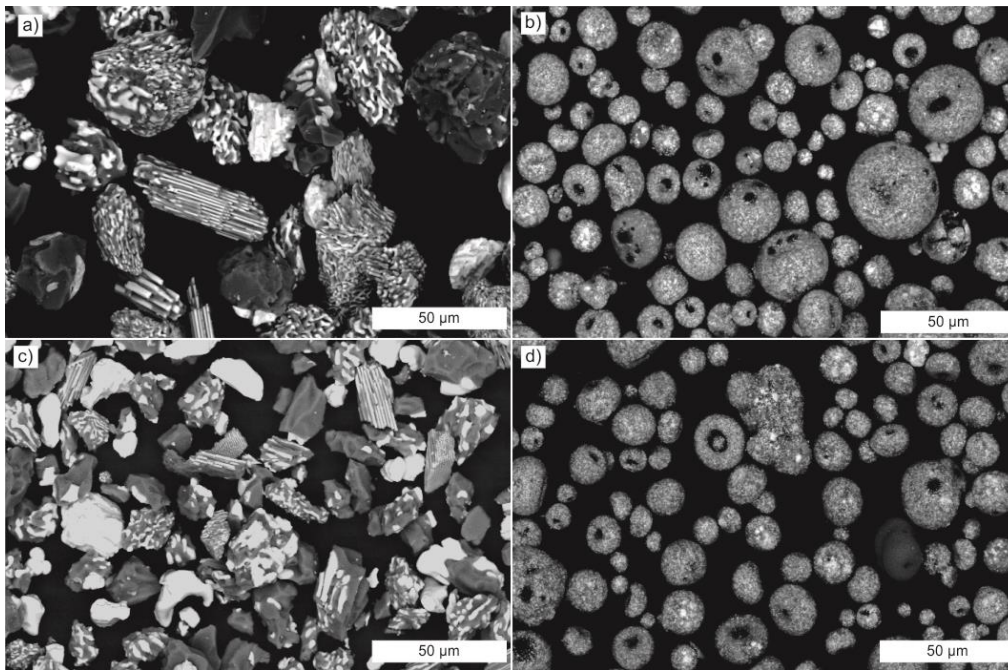


Fig. 3 Powder morphologies of a) APS F&C; b) APS A&S; c) HVOF F&C; and d) HVOF A&S powders. SEM (BSE)-images.

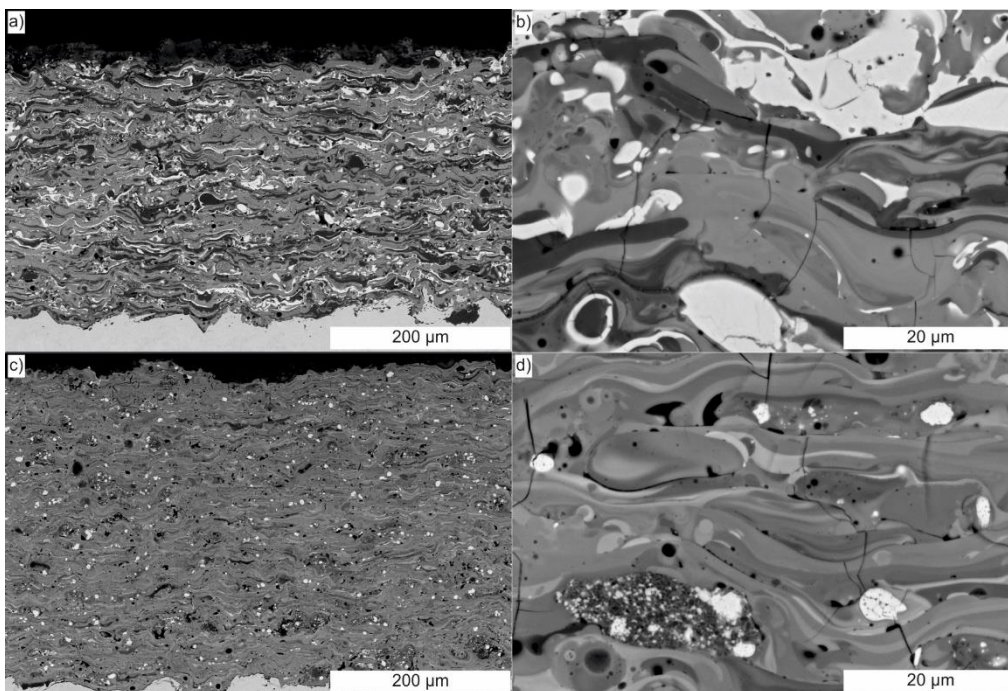


Fig. 4 APS F&C  $\text{Al}_2\text{O}_3$ -40ZrO<sub>2</sub> coating a) structure and b) microstructure and APS A&S  $\text{Al}_2\text{O}_3$ -40ZrO<sub>2</sub> coating c) structure and d) microstructure. SEM images.



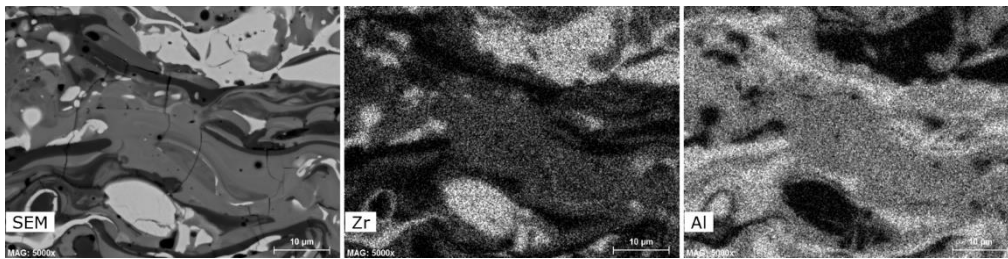


Fig. 5 EDS elemental map of APS F&C coating presenting the difference in elemental content within the coating. The light color illustrates areas rich in the element in question.

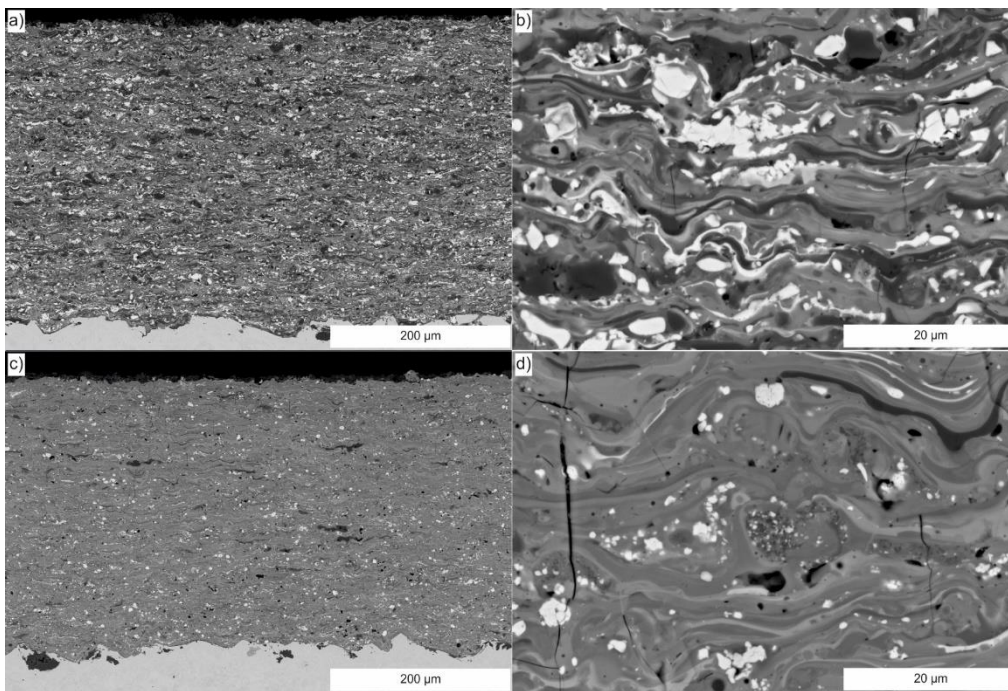


Fig. 6 HVOF F&C  $\text{Al}_2\text{O}_3\text{-40ZrO}_2$  coating a) structure and b) microstructure and HVOF A&S  $\text{Al}_2\text{O}_3\text{-40ZrO}_2$  coating c) structure and d) microstructure. SEM images.

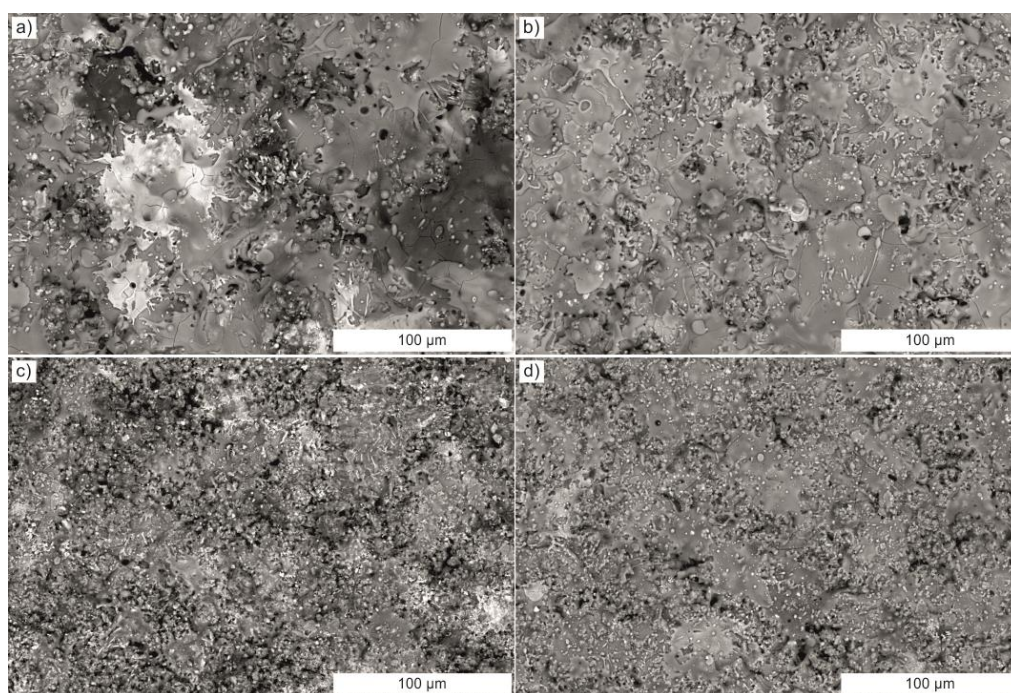


Fig. 7. Surface images of the coatings. APS a) F&C b) A&S and HVOF c) F&C and d) A&S. SEM-images.

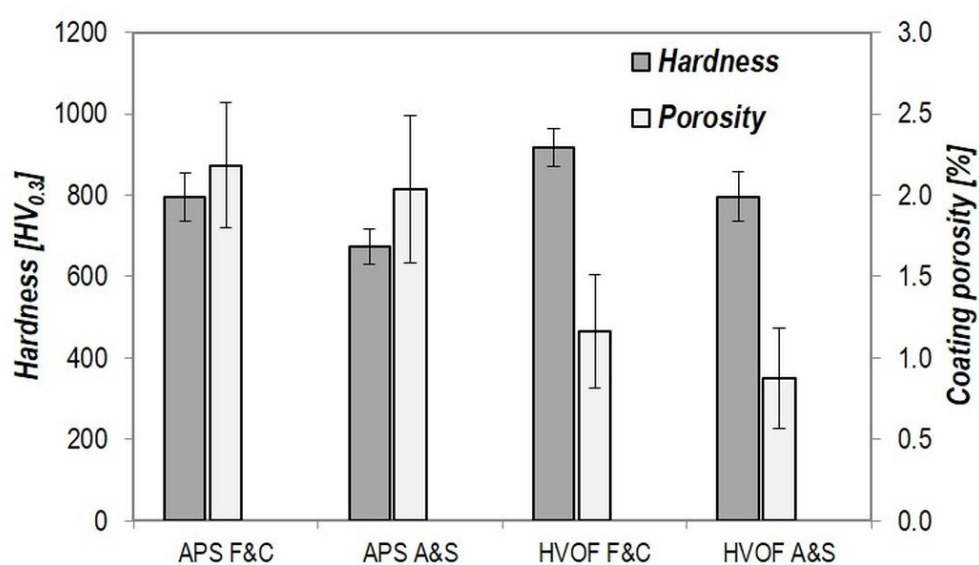


Fig. 8. Vickers hardness and porosity obtained from the coating cross-sections



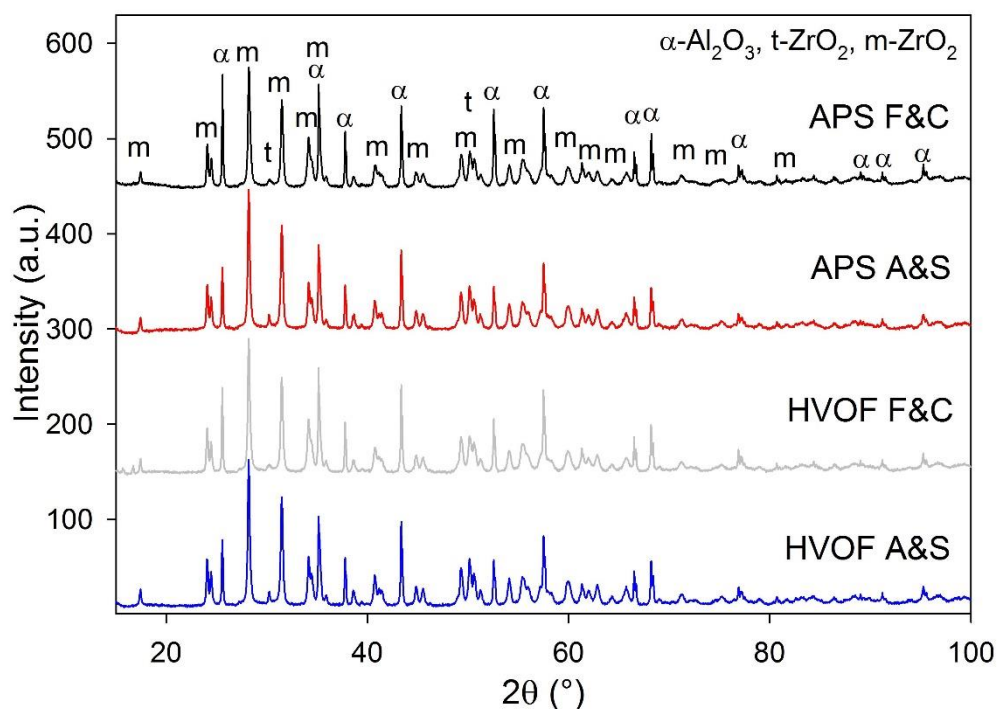


Fig. 9 XRD scans of the feedstock powders with the peaks of the different phases denoted by symbols.

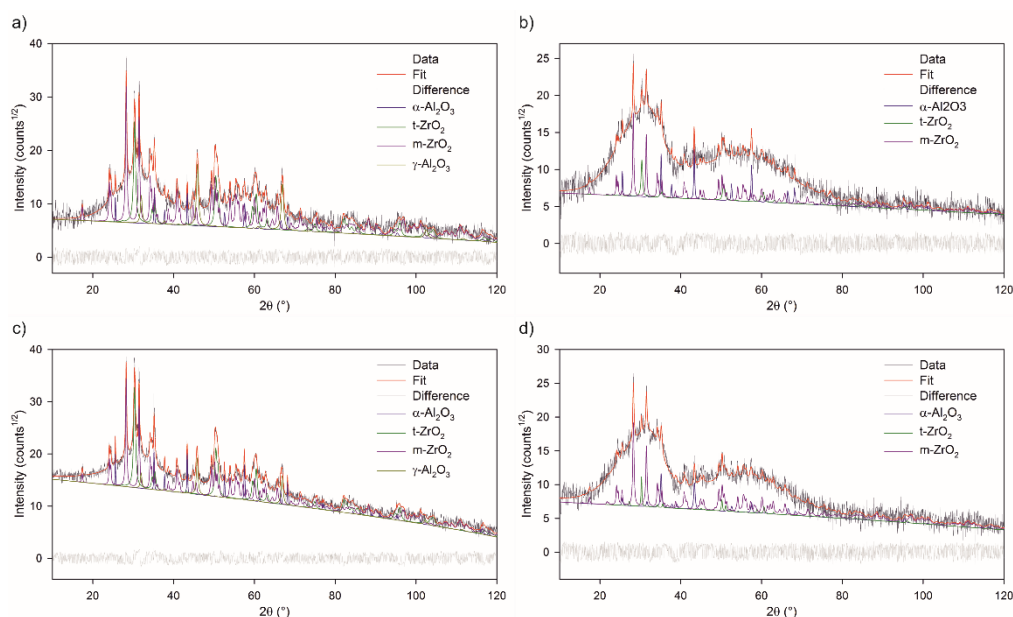


Fig. 10. Rietveld fits of the x-ray diffraction patterns of the coatings: a) APS F&C, b) APS A&S, c) HVOF F&C, d) HVOF A&S.

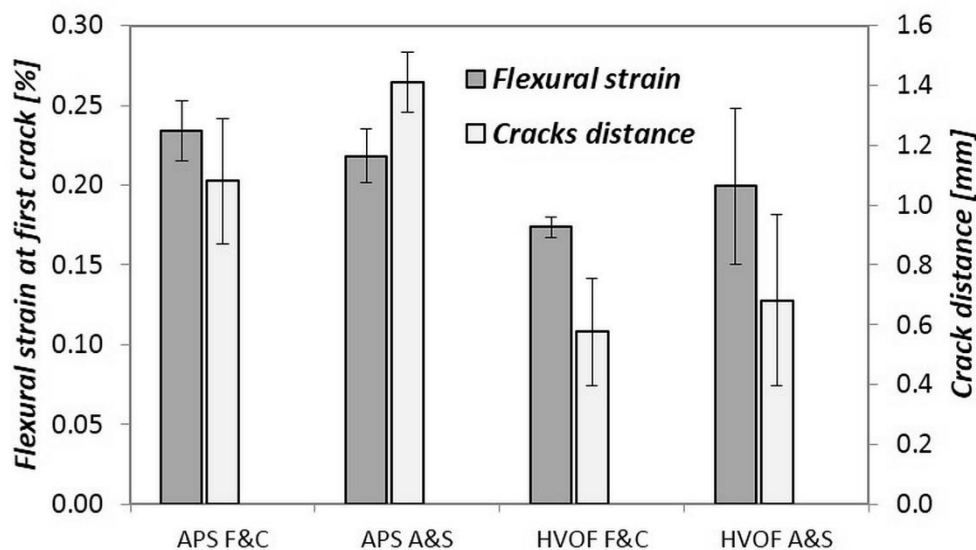


Fig. 11. Flexural strain and spacing between major through-thickness cracks as evaluated from in-situ experiment.

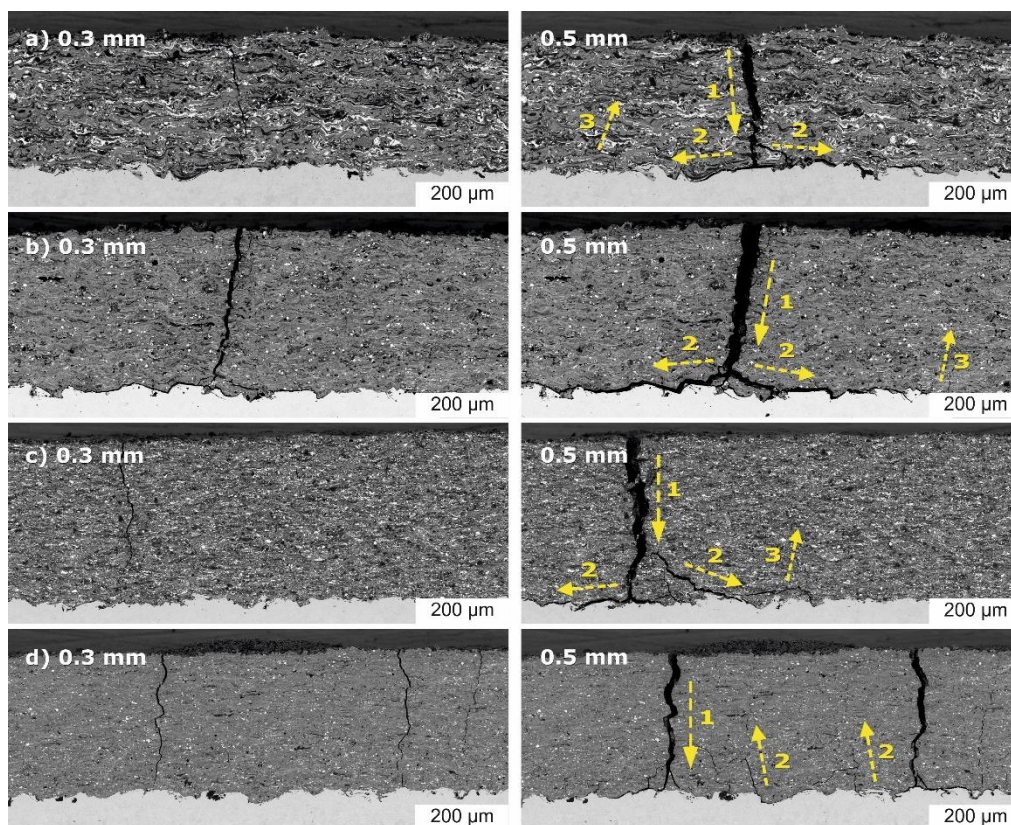


Fig. 12. Failure evolution during in-situ observation of the three-point bending of APS a) F&C, b) A&S and HVOF c) F&C, d) A&S coatings. Displacement of the central support 0.3 mm (left) and 0.5 mm (right). Arrows show the direction and propagation of the cracks. Numbers denote the order of appearance of cracks.

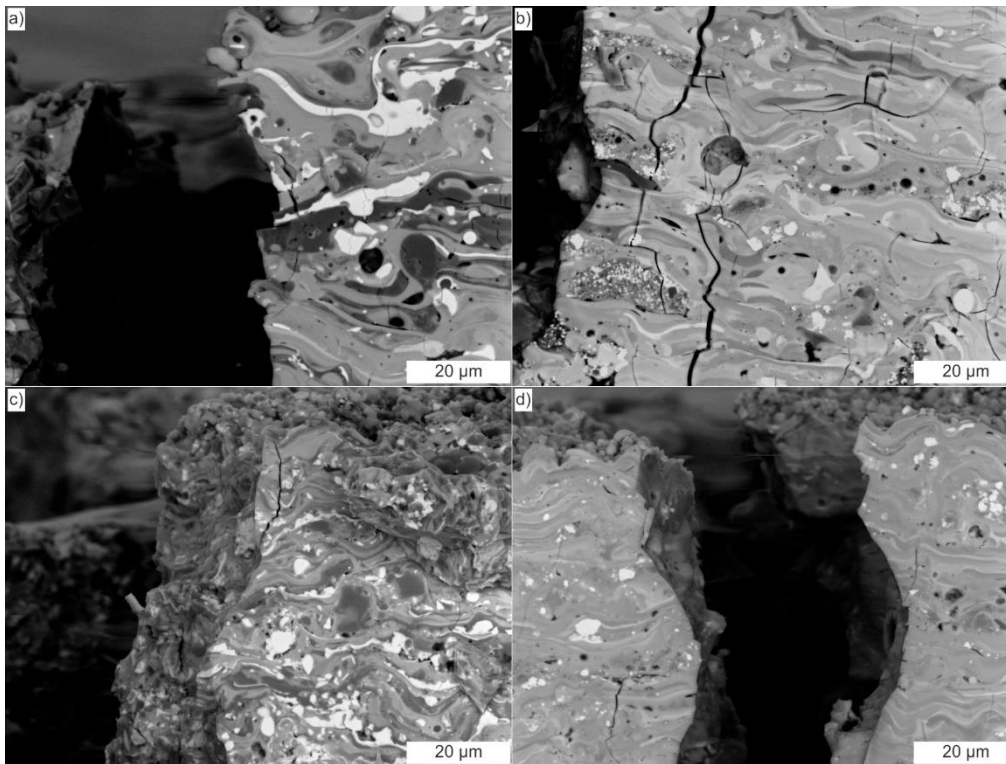


Fig. 13 Detailed SEM-images of the crack propagation after in-situ bending in a) APS F&C, b) APS A&S, c) HVOF F&C and d) HVOF A&S –coatings.

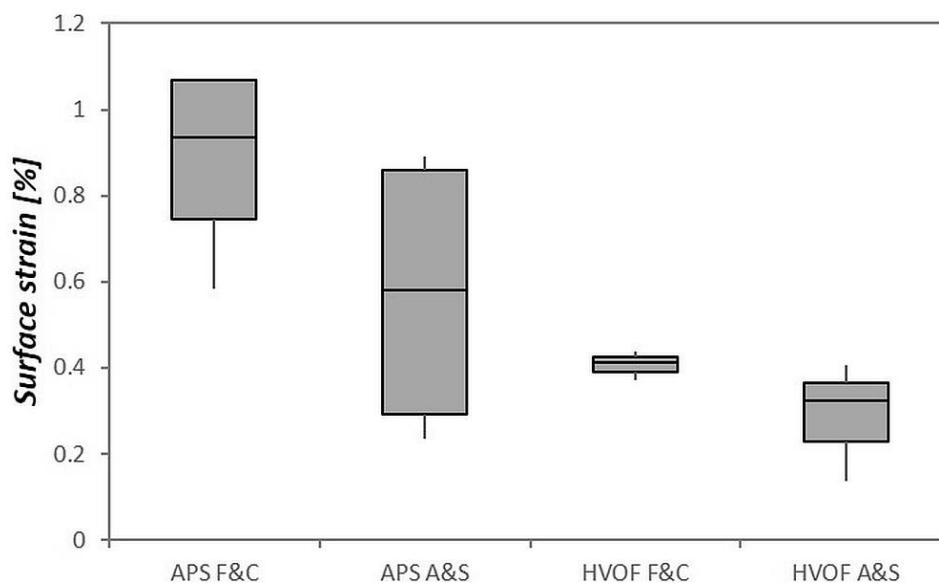


Fig. 14. Box-plot of the surface strain at the point of theoretical fracture, as measured by AE-instrumented four-point bending.

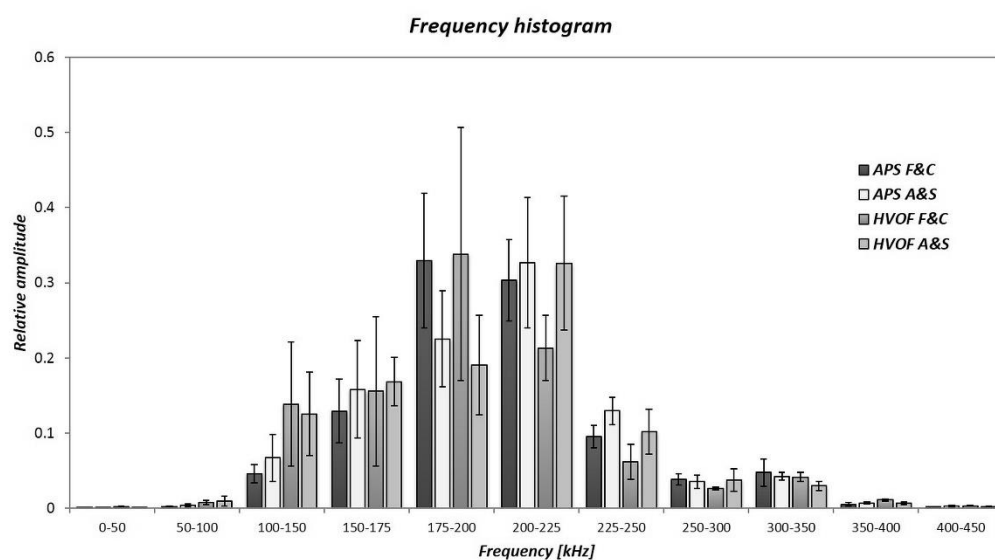


Fig. 15. A normalized histogram of the average power density spectra of the coating samples describing differences in the characteristic frequencies.